ROYAL SOCIETY OF CHEMISTRY

PAPER

Check for updates

Efficient NIR-to-vis photon upconversion in binary rubrene films deposited by simplified thermal evaporation†

Edvinas Radiunas, [ID] [a] Lukas Naimovičius, [ID] [a] Steponas Raišys, [ID] [a] Augustina Jozeliūnaitė, [b] Edvinas Orentas [ID] [b] and Karolis Kazlauskas [ID] *[a]

Low-power NIR-to-vis upconversion (UC) of incoherent excitation mediated by triplet–triplet annihilation (TTA) has a variety of promising applications, *e.g.* in photovoltaics; however, these are strongly hampered by low UC efficiency in the solid state. The issue is mainly related to the most efficient rubrene annihilator (emitter) utilized for this spectral range, which experiences severe concentration quenching in films due to singlet fission (SF). Herein, a simplified thermal evaporation technique is introduced to alter the morphology of binary rubrene films without involving a singlet sink aiming to suppress SF and boost UC efficiency. Hot-plate evaporation of rubrene under ambient nitrogen on a Peltier-cooled substrate pre-coated with a sensitizer layer is demonstrated to significantly improve the FL quantum yield and triplet energy transfer after annealing, subsequently ramping UC quantum yield up to $(1.2 \pm 0.15)\%$ (out of maximum 50%). This is at least twice as high as that found in any other binary NIR-UC film reported so far. Moreover, we find that the statistical probability (f factor) of producing a singlet from two triplets *via* TTA in amorphous rubrene films ($f = 19.5\%$) is close to that estimated for rubrene in a solution. This finding infers a maximum UC yield of $1/2 \times f \approx 10\%$ and explains why there are no reports on rubrene UC systems exceeding this value.

Introduction

Growing research interest in photon energy upconversion (UC) attainable in organic materials *via* triplet–triplet annihilation (TTA) is stimulated by promising applications in photocatalysis,[1–3] bioimaging,[4] photovoltaics,[5–14] targeted drug delivery,[15,16] *etc.*[17–19] The inherent ability of TTA-UC to be driven by incoherent irradiation and at low power densities ($\sim$ mW cm^{-2})[5,7,20] implies great opportunities for solar energy harvesting, since poorly utilized near-infrared (NIR) photons in solar cells can be readily converted into the visible radiation and reused thereafter for photocurrent generation.[5,7] The general energy scheme depicting energy transfer processes in a typical TTA-UC system is shown in Fig. 1. Usually, TTA-UC is realized in binary systems composed of a sensitizer and an annihilator (emitter). The sensitizer is responsible for low energy photon absorption into the singlet state, conversion of

the singlet excitation to triplet *via* intersystem crossing (ISC) and triplet energy transfer (TET) to the emitter. Meanwhile, the emitter ensures triplet migration until the two of them meet, promoting one of the triplets to a higher-energy singlet state *via* TTA. The whole process is finalized by the UC emission from the singlet state. Considering that each intermediate energy transfer step contributes to the UC quantum yield (ϕ_{UC}), it can be expressed as[14,21,22]

$$\phi_{UC} = \frac{1}{2} f \phi_{ISC} \phi_{TET} \phi_{TTA} \phi_{FL} . \qquad (1)$$

Here f is a statistical factor representing the probability of obtaining a singlet from two triplets *via* TTA.[14,22–24] ϕ_{FL} is a fluorescence quantum yield of an emitter. We note that the maximum ϕ_{UC} is limited to 50%, because during the TTA, at most one UC photon can be produced per two absorbed ones.[21,25]

Challenging practical TTA-UC applications, such as in photovoltaics, demand high NIR-to-vis UC efficiency, preferably in the solid state.[8,26] A fulfilment of the latter requirement remains an important issue that many research groups aim to overcome. It is evident that the vast majority of demonstrated solid-state UC systems operating in the NIR range (>700 nm) usually express very low ϕ_{UC}, typically $<1\%$.[14,26–32]

[a] *Institute of Photonics and Nanotechnology, Vilnius University, Saulėtekio av. 3, LT-10257 Vilnius, Lithuania. E-mail: karolis.kazlauskas@ff.vu.lt*

[b] *Institute of Chemistry, Faculty of Chemistry and Geosciences, Vilnius University, Naugarduko 24, LT-03225 Vilnius, Lithuania*

† Electronic supplementary information (ESI) available. See DOI: 10.1039/d1tc05332a

Fig. 1 TTA-UC energy scheme of Rub/PdPc with the corresponding energy transfer processes. ISC – intersystem crossing, TET – triplet energy transfer, TTA – triplet–triplet annihilation, SF – singlet fission, UC – upconversion.

Commonly exploited TTA emitters for the NIR spectral range are tetracenes,[33–35] rubrenes,[24,30,31,36–40] perylenes[26,41] or diketopyrrolopyrroles.[42] Most of these emitters are efficient in the liquid environment. Meanwhile, there is a lack of emitters with a low lying triplet-state that are fluorescent in the solid state.[14] The best-performing NIR-to-vis UC systems demonstrated so far, both in solution and the solid state, rely on the rubrene (**Rub**) emitter.[14]

Previously, we demonstrated that in the **Rub**-based UC solutions ϕ_{UC} is limited to ~7.8% due to the relatively low f factor (~15.6%).[22] In the solid-state, however, **Rub** additionally suffers from severe concentration quenching mainly attributed to singlet fission (SF), which results in a more than 60-fold drop in the fluorescence quantum yield (ϕ_{FL}). Thus, even the most efficient **Rub**-based UC films typically demonstrate one or two orders of magnitude lower ϕ_{UC} compared to those of UC solutions, where ϕ_{FL} of **Rub** is almost unity.

Generally, SF related losses can be mitigated by using two approaches, *i.e.* (i) molecular engineering, which relies on the chemical modification of the existing emitters or the introduction of alternative ones; and (ii) physical engineering based on altering the UC film composition or morphology.

Previously, we utilized a molecular engineering approach to introduce *t*-butyl substituents into **Rub** and improve the NIR-to-vis ϕ_{UC} in the solid films.[43] It was also revealed that **Rub** modifications at the periphery do not inhibit TTA step; however, substituents linked directly to the tetracene core suppress TTA dramatically.[44] The standard physical engineering approach to combat low ϕ_{FL} in **Rub** films and mitigate SF is to introduce the third component, *i.e.* a singlet exciton sink (collector), dibenzotetraphenylperiflanthene (DBP). Doping **Rub** films with a low concentration of DBP was reported to boost ϕ_{FL} by a factor of 20 due to the efficient FRET of

upconverted singlets from **Rub** to DBP.[27,45] Yet, the potential for altering the UC film morphology by employing different preparation techniques to address low ϕ_{UC} issues was not exploited to the fullest extent.

In this work, we demonstrate the potential of the physical engineering approach to boost the UC efficiency in the binary emitter/sensitizer films without involving an exciton sink. To prepare UC films, we introduce a simplified thermal evaporation technique (using a hot plate) in an inert atmosphere. The highly concentrated **Rub** films obtained in this way display an order of magnitude higher fluorescence quantum yield (ϕ_{FL}) compared to the films produced by solution-processing or sophisticated thermal deposition in a vacuum. Furthermore, we show that in these films the sensitizer and emitter are well dispersed and intermixed to result in an efficient triplet energy transfer (ϕ_{TET}). The improved ϕ_{FL} along with the efficient ϕ_{TET} results in a record-high ϕ_{UC} of the **Rub**-based binary solid-state systems, which is at least twice as high as that obtained in any other binary NIR-UC film reported so far.[14,32,46]

Experimental

Materials

Rubrene (**Rub**) was purchased from TCI. Polystyrene (PS) was purchased from Sigma-Aldrich. The synthesis of palladium phthalocyanine (**PdPc**) was published elsewhere.[22]

Optical techniques

The absorption spectra of the investigated samples were recorded using a UV-vis-NIR spectrophotometer Lambda 950 (PerkinElmer). Fluorescence (FL) of the samples was excited at 485 nm either by using a 150 W xenon arc lamp (Oriel) coupled to a monochromator (Sciencetech), or by utilizing a continuous-wave semiconductor laser diode (Picoquant). Photon upconversion (UC) was induced by exciting at 730 nm using a 12 mW power continuous-wave semiconductor laser diode (Picoquant). Steady state FL and UC emission spectra were measured using a back-thinned CCD spectrometer PMA-12 (Hamamatsu). Fluorescence transients of the samples were measured by using a time-correlated single photon counting system PicoHarp 300 (Picoquant), which utilized a pulsed semiconductor laser diode (wavelength – 485 nm, pulse duration – 70 ps, repetition rate – 1 MHz) as an excitation source. Phosphorescence spectra in the NIR range were measured using a water-cooled iDus InGaAs 1.7 array detector (Andor). FL quantum yields (ϕ_{FL}) were estimated by utilizing an integrating sphere (Sphere Optics) coupled to the CCD spectrometer PMA-12 *via* an optical fiber; the xenon arc lamp was used as an excitation source. ϕ_{UC} was estimated by comparing the integral of the UC spectrum with that of the FL spectrum of the **PdPc** sensitizer with known quantum yield, as described previously.[22] For strong UC signals both integrating sphere and comparative methods were used to ensure the reliability of the obtained values.

This journal is © The Royal Society of Chemistry 2022

J. Mater. Chem. C, 2022, **10**, 6314–6322 | **6315**

Results and discussion

Due to the low-lying triplet state (T_1) in the NIR region and $2 \times T_1$ close to the singlet energy (S_1) in the visible range, **Rub** became the standard emitter for NIR-to-vis photon upconversion.[14,27,28,31,32,47,48] In fact, by far there are almost no alternative emitters capable of delivering comparable performance in the solid-state.[14] Even though solution-processed **Rub** neat films have low ϕ_{FL} ($\sim 1\%$), other similar TTA emitters with low triplet energy ($T_1 < 1.2$ eV) are almost non-emissive, because of aggregation-caused quenching. Low ϕ_{FL} is disastrous, as it subsequently reduces ϕ_{UC} (eqn (1)). One of the main causes of low ϕ_{FL} in **Rub** films is singlet fission (SF), which is feasible due to the favorable energetics ($S_1 \approx 2 \times T_1$) of **Rub**. Lasting on a time-scale of picoseconds SF outcompetes radiative decay by opening the alternative deactivation channel for the singlets, *i.e.* splitting into two triplets. Depending on the local molecular environment, the emerged triplet pairs can rapidly undergo geminate triplet fusion or dissociate and either (i) decay non-radiatively, or (ii) diffuse and form encounter complexes at a much slower rate for non-geminate TTA.[23,45,49,50]

It is well known that SF-associated losses are strongly related to the degree of crystallinity of the **Rub** films. The crystallinity can be altered by varying film preparation conditions and probed by monitoring their optical properties.

To minimize SF, amorphous **Rub** films with a chaotic molecular orientation and large average intermolecular distance must be produced. Biaggio *et al.* successfully exploited molecular beam deposition in a high vacuum to obtain amorphous **Rub** films.[50] The films were virtually free from SF and showed mono-exponential fluorescence decay ($\tau = 16.4$ ns) close to that of **Rub** in solution.[50]

In the current study, diverse deposition conditions of emitter **Rub** are investigated to assess the impact of emitter morphology on ϕ_{FL}, and correspondingly ϕ_{UC} in the solid films. Featuring an appropriate energy level alignment, palladium phthalocyanine (**PdPc**) was chosen as a triplet sensitizer for the **Rub**.[43] Fig. 2a and b illustrates the step-by-step fabrication of UC films under investigation. In the first step, the sensitizer layer composed of an optically inert polymer matrix doped with low concentration (0.1 wt%) of **PdPc** was formed by spin-coating (Fig. 2a). Then **Rub** was deposited on top by using one of the four distinct thermal evaporation modes to result in the formation of the UC film (Fig. 2b). In the vacuum deposition mode, controlled thermal evaporation in a high vacuum ($\sim 10^{-7}$ Torr) was used. This mode was previously reported to produce amorphous rubrene films and therefore served as a reference deposition mode.[50] The remaining three modes were based on a simplified thermal evaporation of **Rub** (using the hot-plate) in ambient nitrogen. In the cold deposition mode, rubrene molecules were deposited on a Peltier cooled (-10 °C) substrate (Fig. 2b). This mode is expected to instantly freeze emitter molecules on the substrate, thus producing amorphous films. Aiming to quantify the effect of substrate cooling, cold-deposited films were annealed at 100 °C defining the post-annealing mode. Lastly, **Rub** evaporation on an uncooled substrate (naturally heated due to the close proximity of the evaporation source) was named the hot deposition mode.

The UC films prepared at different conditions were initially evaluated by measuring FL transients and ϕ_{FL} (Fig. 3). The results clearly show high sensitivity to the **Rub** deposition mode. The FL transients consisted of the dominant prompt decay (fractional contribution of 70–90% to an overall decay) affected by SF and the minor slower decay component resembling natural decay of the isolated **Rub** species. The prompt
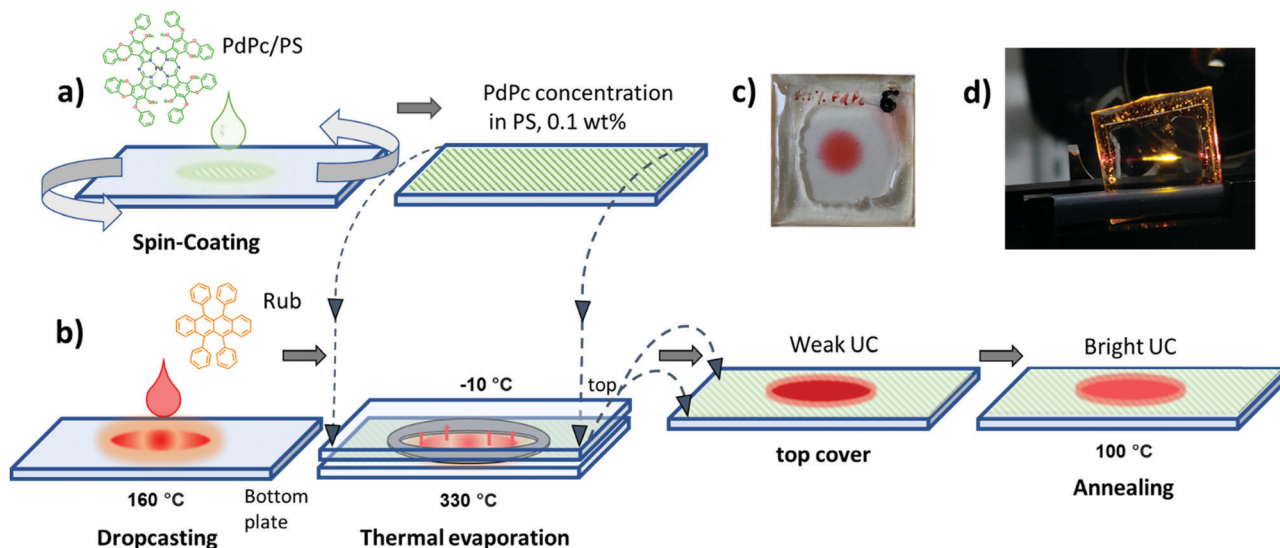

Fig. 2 Preparation of UC films. (a) Formation of sensitizer (**PdPc**)-doped PS layer by spin-coating; (b) deposition of emitter (**Rub**) by drop-casting stock solution (1 mg ml^{-1}) on a glass substrate followed by thermal evaporation of **Rub** on actively cooled (previously prepared) sensitizer layer (depicted as top glass). The final UC film is obtained by thermal annealing; (c) photo of the final UC film with the encapsulating epoxy visible on the edges; and (d) the UC film excited with a 730 nm CW laser.

6316 | *J. Mater. Chem. C*, 2022, **10**, 6314–6322

This journal is © The Royal Society of Chemistry 2022

Fig. 3 FL transients of **Rub** films deposited on top of the sensitizer layer using different thermal evaporation modes (specified). Lines represent single-exponential fits of the dominant prompt decay components. FL lifetimes and quantum yields indicated.

Fig. 4 **PdPc** phosphorescence spectra of the cold-deposited UC film before (circles) and after (triangles) annealing, and of the reference emitter-free film (solid line). TET{**PdPc** → **Rub**} efficiency of the untreated as well as annealed film is indicated. The inset schematically illustrates the UC film before and after annealing.

component was described by a single-exponential decay profile to determine excited state lifetime. The shorter FL lifetime suggested an enhanced SF, and hence, a reduced ϕ_{FL}.

In the case of vacuum-deposited films, rapid decay with $\tau = 2$ ns and low ϕ_{FL} (1.6%) was obtained. This was unexpected, since a vacuum-deposition previously was reported to result in amorphous films[50] free from SF and with the FL lifetime similar to that of Rub in solution ($\tau = 16.4$ ns).

Interestingly, prolonged decay ($\tau = 3.8$ ns) as well as increased ϕ_{FL} up to 8.5% was obtained for the films fabricated using the cold deposition mode, indicating a more random molecular orientation and suppressed SF. Post-annealing of the UC films further extended the FL lifetime to 8.5 ns and improved ϕ_{FL} by almost 2-fold. Finally, the highest ϕ_{FL} of 20.5% along with the longest FL lifetime ($\tau = 12$ ns) was determined for the films prepared in the hot deposition mode.

At first glance, the role of the heat treatment introduced during the film annealing or hot deposition is counterintuitive, since this is anticipated to facilitate **Rub** crystallization.[51] Excess energy supplied in the form of heat may suffice to rearrange and crystallize **Rub** causing the formation of non-radiative SF centers. We note that the annealing temperature was set to correspond to the glass transition temperature (T_g) of the PS polymer employed. However, excess heat during the annealing can also promote **Rub** diffusion into the bottom sensitizer layer thereby diluting it and suppressing aggregation-caused FL quenching (see the inset of Fig. 4). Likewise, the hot deposition mode may result in a deeper **Rub** diffusion and thus stronger dilution more resembling the behavior of isolated **Rub** species or that of the purely amorphous film.

Further investigation in support of molecular diffusion involved studying the UC properties of the films *via* NIR excitation (730 nm) of the sensitizer. The improvement of UC efficiency was expected to be in correspondence with that of

ϕ_{FL}. Indeed, the films of the lowest ϕ_{FL} fabricated using vacuum deposition and cold deposition modes exhibited barely detectable UC. On the other hand, annealed and hot-deposited films displayed bright UC. This result can be rationalized by considering the differences in the triplet energy transfer efficiency ϕ_{TET} (eqn (1)). The big temperature contrast during the cold deposition implies the formation of a bilayer UC film featuring a distinct boundary between the sensitizer and the emitter. As a result, most of the sensitizer triplets are generated far from the emitter species implying that short-range Dexter-type TET can only occur in a narrow interface region. Meanwhile, the promoted molecular diffusion during the film annealing causes mixing of the sensitizer and the emitter, thus reducing intermolecular separation and enhancing TET{**PdPc** → **Rub**}. Scanning electron microscopy (SEM) images supporting the mixing of the sensitizer and the emitter after annealing are provided in ESI† (see Fig. S1 and S2 and explanation therein). The mixing was also verified by evaluating ϕ_{TET}, where we compared phosphorescence intensity from the sensitizer **PdPc** of the cold deposited UC films with the same films after annealing (Fig. 4). For reference, we also measured phosphorescence of the emitter-free film containing only the sensitizer layer (polymer doped with **PdPc**). The experimental conditions ensured identical concentrations of **PdPc** and the sensitizer layer thickness of the tested films, thus enabling the intermixing effect of **Rub** and **PdPc** on TET to be addressed explicitly. The most intense **PdPc** phosphorescence peaked at 1106 nm was observed for the emitter-free film, since no TET{**PdPc** → **Rub**} was possible. Cold-deposited films expressed just a slightly reduced phosphorescence intensity due to inefficient ϕ_{TET}, whereas this intensity for the annealed films was severely decreased as a result of enhanced TET{**PdPc** → **Rub**}. Considering that

$$\phi_{TET} = 1 - \frac{I}{I_0}, \qquad (2)$$

where I and I_0 are the phosphorescence intensities of the studied and the reference (emitter-free) films, respectively,[22,32] we estimated that ϕ_{TET} in the cold deposited UC films is up to 11%, whereas it reaches 60% in the annealed films. The obtained ϕ_{TET} in the annealed films was verified by performing phosphorescence measurements in the integrating sphere (see Fig. S3, ESI†). In this way, the light scattering effects of the films impacting the light outcoupling could be taken into account.

Spatial variations of **PdPc** phosphorescence intensity and ϕ_{TET} in the annealed films are presented in the ESI† (see Fig. S4 and explanation therein). Taking into account the simplified thermal evaporation technique employed for the fabrication of the UC films, the reproducible ϕ_{TET} values could be obtained within the central area of ~ 4 mm in size.

Even though the most efficient ϕ_{FL} was achieved using the hot deposition mode of **Rub**, the UC films prepared in this way had poor reproducibility. Specifically, **Rub** films were determined to be very sensitive to growth time and exhibited rapid crystallization already in the first growth stages (Fig. S5, ESI†). The morphological changes were accompanied by drastic spectral and FL decay time variations, *i.e.*, additional aggregate-related FL band started emerging at 740 nm and τ reduced from 5.3 ns to 0.27 ns indicating increasing domination of SF.

Taking into account the reproducibility issues in the hot-deposition mode, further UC performance optimization was carried out for the films prepared by cold deposition followed by annealing. This deposition mode permitted control of the **Rub** thickness avoiding crystallization and allowed for consistent results (Fig. S6a, ESI†). Unlike neat **Rub** films obtained by the same method and showing increasing crystallization within a few weeks after fabrication, UC films fabricated by depositing **Rub** on top of the sensitizer-doped polymer layer followed by annealing were found to be stable. No signs of crystallization were detected several months after fabrication (see Fig. S7, ESI†) where FL lifetimes of the films are shown to remain constant at least within 240 days after film deposition). We attribute this to the dilution of **Rub** within the polymer layer, and thus suppression of rubrene aggregation.

Rub film thickness of approximately 600 nm, which corresponded to 3 min evaporation time was found to be optimal based on the UC intensity measurements (Fig. S6b, ESI†). Post-annealing of the films performed at 100 °C for ~ 5 min yielded good film uniformity and bright UC emission, whereas longer annealing durations as well as higher temperatures induced strong crystallization (see Fig. S8, ESI†), and thus, were unacceptable for the UC film fabrication.

In the following UC optimization step, different sensitizer concentrations were tested while maintaining identical **Rub** deposition conditions (Fig. 5). Clearly, the increasing sensitizer concentration from 0.1 wt% to 5 wt% reduced the UC signal by 5 times suggesting enhanced upconverted energy back-transfer from **Rub** to **PdPc**. Although a higher sensitizer concentration is supposed to improve NIR absorption and reduce UC threshold, densely packed sensitizer molecules facilitate energy back-transfer diminishing the overall ϕ_{UC}.[52] Aiming to maximize UC efficiency, the lowest **PdPc** concentration (0.1 wt%) was

Fig. 5 UC emission spectra of **PdPc**/PS/**Rub** films with different **PdPc** concentrations. The spectra are normalized to the **PdPc** fluorescence maximum at 774 nm. **Rub** deposition conditions and **PdPc**-doped PS layer thickness (260 nm) were maintained the same. Excitation, 730 nm CW laser. A notch filter was used to suppress scattered excitation.

selected for further optimization. In fact, even lower concentration should potentially lead to a higher ϕ_{UC}; however, the subsequently decreased sensitizer absorption and thereby significantly weakened UC signal would compromise reliability of the results.

In the next step, the uniformity of the rubrene film deposited on top of **PdPc**-doped PS (sensitizer layer) was investigated. The measurements were carried out for different sensitizer layer thicknesses enabling the optimal one for maximal UC performance to be revealed. As discussed above, well mixed sensitizer and emitter films are required to have efficient ϕ_{TET} as well as high ϕ_{FL} of **Rub**. By assuming limited **Rub** diffusion into the sensitizer layer during the annealing, the too thick sensitizer layers could cause high absorption, yet likely reduced ϕ_{UC} due to lowered ϕ_{TET}. To verify this, we prepared a series of spin-coated sensitizer layers of different thickness, which was varied by altering mixture viscosity and spin coater speed. The film thickness was probed using AFM (see Fig. S9, ESI†). The **Rub** was deposited on top of the sensitizer layer through a circular metal spacer, forming a disk-shaped film (see the inset of Fig. 6). The prepared UC films were investigated by scanning across the surface in the x direction with the focused 730 nm laser beam and collecting the emission spectra as illustrated in Fig. 6.

The detailed scheme of this experiment is presented in Fig. S10 (ESI†). The measured spectra were analysed by discerning UC and FL_{PdPc} spectral components peaking at 560 nm and 774 nm, respectively, and examining they relative intensities. Prior to FL_{PdPc} analysis, the strong background signal due to the scattered excitation light and UC emission tail was subtracted.

The UC intensity was found to exhibit a steep increase by almost 3 orders of magnitude with the excitation spot moving
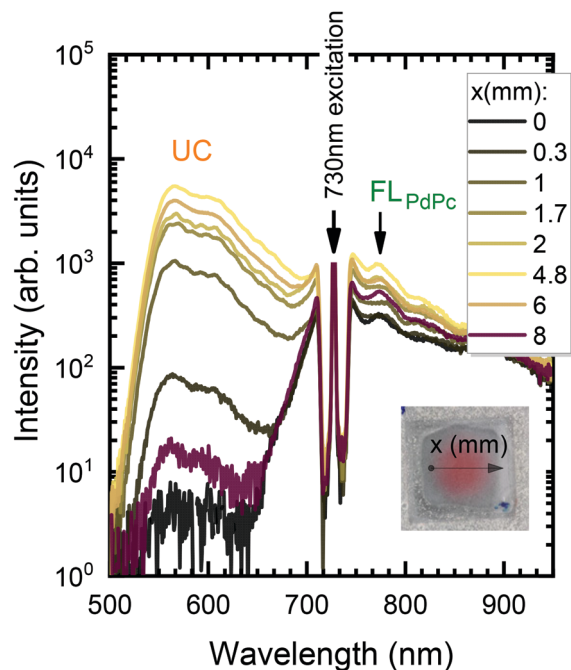
6318 | *J. Mater. Chem. C*, 2022, **10**, 6314–6322

This journal is © The Royal Society of Chemistry 2022

Fig. 6 Semi-log plot of UC emission spectra of PS:**PdPc**/**Rub** film measured at different excitation spots along x direction (indicated). Excitation, 730 nm. **PdPc** concentration in PS, 0.1 wt%. Sensitizer layer thickness, 110 nm. A picture of UC film is shown in the inset.
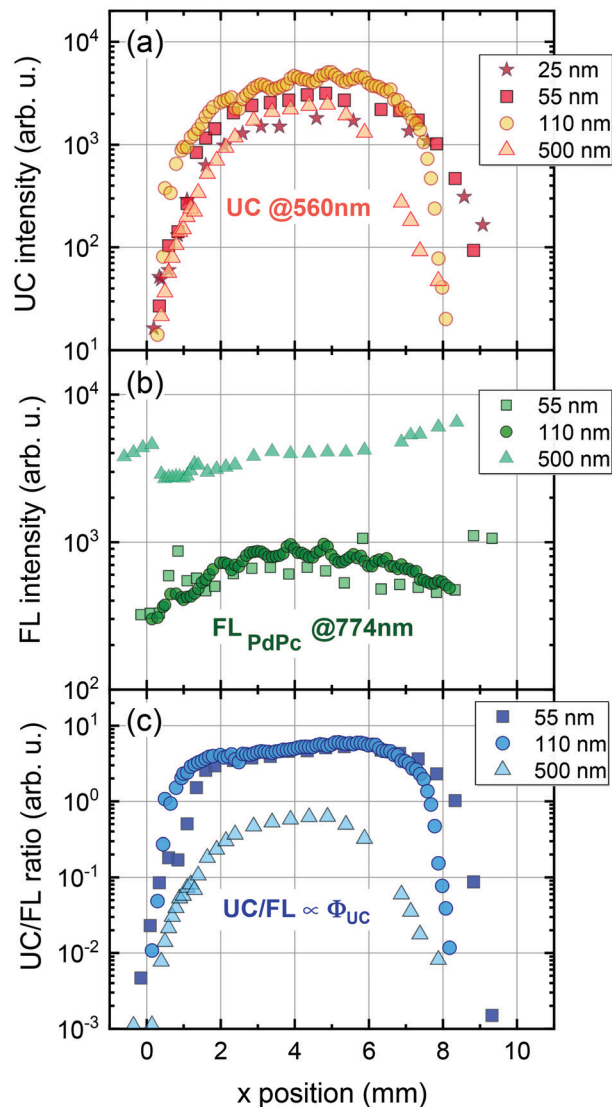

Fig. 7 (a) UC intensity at 560 nm, (b) FL intensity of **PdPc** at 774 nm and (c) UC/FL intensities ratio for different sensitizer layer thickness (indicated). Excitation, 730 nm. **PdPc** concentration in PS, 0.1 wt%. Each measurement was performed under the same conditions.

from the film edge to the centre (Fig. 7a). The intensity profile resembled Gaussian-like thickness distribution of the evaporated **Rub** and suggested that some critical thickness of the emitter is required to promote TTA in the **Rub** layer. Additionally, the sensitizer layer thickness of 110 nm was determined to be the optimal as giving rise to the highest UC intensity at these deposition conditions. Spatial distribution of FL intensity emanating from **PdPc** was found to be much more flat (Fig. 7b) in agreement with rather homogeneous sensitizer layers formed by spin-coating. These layers contained roughly the same amount of **PdPc** across the scanned area implying insignificant FL intensity variation *vs* the excitation coordinate. Taking into account that $FL_{\textbf{PdPc}}$ is not affected by the presence of **Rub** due to the energy level alignment, $FL_{\textbf{PdPc}}$ intensity should be proportional to the sensitizer layer thickness and **PdPc** concentration. Since the latter was fixed at 0.1 wt%, the thicker sensitizer layers (as more absorbing 730 nm radiation) resulted in the higher $FL_{\textbf{PdPc}}$ intensity. Importantly, considering that ϕ_{FL} of **PdPc** is constant across the film, this intensity can be used as an internal reference for the UC signal, thereby enabling the judgement of ϕ_{UC} from the UC and $FL_{\textbf{PdPc}}$ intensity ratio (Fig. 7c). For instance, although 25 nm and 500 nm-thick films showed similar UC intensity, the thicker films exhibited higher $FL_{\textbf{PdPc}}$ intensity correspondingly implying lower ϕ_{UC}. Unfortunately, the $FL_{\textbf{PdPc}}$ signal of 25 nm films was too weak to be measured; however, the data presented in Fig. 7c clearly suggest that thin sensitizer layers are more favorable for the realization of high ϕ_{UC}.

We note that the UC films with thin sensitizer layers ($<$100 nm) were difficult to measure as they were highly scattering and featured weak absorption, and hence, a relatively low UC intensity. These layers acted as a buffer for evaporated **Rub** and had a significant influence on the final UC film morphology. During the **Rub** deposition thin buffer experienced partial melting thereby forming a rough surface with enhanced scattering of the incident radiation. Taking this into account, a sensitizer layer thickness of 110 nm delivering one of the highest UC/$FL_{\textbf{PdPc}}$ ratios was selected to be optimal for UC films. Measurement of UC intensity *vs* excitation power density for these UC films enabled to determine the UC threshold of 1.4 W cm^{-2} (Fig. S11, ESI†), which was found to be similar to those of other rubrene-based solid-state UC systems.[27,28,43,46] The optimized UC films were subjected to further evaluation of

Fig. 8 UC spectra of the optimized PS:**PdPc**/**Rub** films with different sensitizer layer thicknesses (indicated). The spectra are normalized to FL$_{\textbf{PdPc}}$ peak intensity (at 774 nm) so that UC intensity would correspond to ϕ_{UC}. Excitation wavelength and density, 730 nm and 100 W cm^{-2}, respectively.

ϕ_{UC} by using the FL$_{\textbf{PdPc}}$ signal as an internal quantum yield reference (Fig. 8) as well as by means of an integrating sphere. The methodological details for the determination of ϕ_{UC} using an internal reference are provided in the ESI.†

Fig. 8 illustrates the UC spectrum of the optimized UC film containing a 110 nm-thick sensitizer layer. Additional spectra of UC films with varying sensitizer layer thickness, prepared under otherwise the same conditions, are also shown for comparison. The UC spectra were normalized to the FL$_{\textbf{PdPc}}$ peak intensity so that UC intensity would correspond to ϕ_{UC}, as discussed earlier. Based on the independent measurements of UC films with different sensitizer layer thicknesses, yet with a fixed **PdPc** concentration of 0.1 wt%, the FL quantum yield of **PdPc** was determined ($\phi_{\text{FL}}^{\text{PdPc}} = 0.1\%$). The reproducibility data of $\phi_{\text{FL}}^{\text{PdPc}}$ tested for different films are included in the ESI.† Essentially, the data confirmed the average $\phi_{\text{FL}}^{\text{PdPc}}$ to be 0.1% with a standard deviation of 0.03%.

Using this value as an internal reference, we could roughly deduce ϕ_{UC} to increase from 0.4% to 1% with decreasing sensitizer layer thickness from 500 to 110 nm (Fig. 8). The obtained ϕ_{UC} were confirmed by the measurements in the integrating sphere, where the most efficient UC film exhibited $\phi_{\text{UC}} = (1.2 \pm 0.15)\%$ (out of maximum 50%).

A slight underestimation of ϕ_{UC} by using an internal reference method can be explained by the strong background signal in the spectral region of FL$_{\textbf{PdPc}}$ due to the intense long-wavelength tail of UC emission. The accurate subtraction of such a strong background is complicated, which results in artificially increased FL$_{\textbf{PdPc}}$ intensity, and subsequently, somewhat reduced ϕ_{UC}. The calculated relative error for ϕ_{UC} in the case of the internal reference method was 32% (see the ESI†) implying that ϕ_{UC} values obtained by both methods agree well within these errors.

ϕ_{UC} of $(1.2 \pm 0.15)\%$ attained in this work represents a 17-fold improvement over our previous spin-coated DBP-doped rubrene films[43] and at least a 2-fold improvement in respect to the most efficient binary rubrene-based solid-state systems reported to date ($\phi_{\text{UC}} \approx 0.3-0.5\%$).[14,29,46]

We also note that the obtained ϕ_{UC} of the binary film approaches the highest efficiency value ($\phi_{\text{UC}} = 2\%$) achieved for the ternary UC film, additionally containing the DBP exciton sink.[46] This reduces the gap in the performance of binary and ternary systems, minimizing the demand for the third component (singlet exciton sink) and stressing the importance of the UC film morphology rather than energetics of individual molecules.

Inserting the maximum efficiency values of the energy transfer/conversion processes determined for our UC films in eqn (1), the probability factor f for rubrene in the solid state can be estimated. Thus, taking into consideration that $\phi_{\text{FL}} = 20.5\%$ (Fig. 3), $\phi_{\text{TET}} = 60\%$ (Fig. 4), and $\phi_{\text{ISC}} = 100\%$ for palladium phthalocyanine-based sensitizers,[22,39,41] $\phi_{\text{TTA}} \approx 100\%$ in the TTA domination regime and that the maximal $\phi_{\text{UC}} = 1.2\%$, the statistical probability f to generate a singlet from two triplets via TTA is 19.5%. The confirmation for the deactivation occurring totally through the second-order path ($\phi_{\text{TTA}} \approx 100\%$) achieved under excitation density of 100 W cm^{-2}, i.e., well exceeding UC threshold is provided in the ESI.†

Interestingly, the obtained f factor is close to that estimated for rubrene in a solution (15.5%).[22] This can be justified by the similar energy level alignment of rubrene in the different environment (solution or amorphous-like film) supporting the finding that the statistical probability of creating a singlet from two triplets via TTA should be in the range of 15–20%. We note that f estimated by us in the TTA-dominating conditions under continuous-wave excitation is 3–4 times lower as compared to that obtained under femtosecond pulsed-laser excitation conditions.[38] The obtained f value implies a maximum ϕ_{UC} of $1/2 \times f \approx 10\%$ for rubrene UC systems, which is reasonable, since no higher ϕ_{UC} has been demonstrated so far.[14,27–32,46,53]

Conclusions

In summary, this work addresses the low UC quantum yield issue in binary emitter/sensitizer films with rubrene serving as the annihilator (emitter). The issue is known to be related to detrimental singlet fission (SF) in highly concentrated rubrene films causing dramatic degradation of the FL quantum yield and subsequent reduction of UC efficiency. To cope with this problem, we offer an altering UC film morphology by exploiting different rubrene deposition techniques so as to suppress SF-promoting rubrene crystallization. From a variety of deposition modes explored, the simplified thermal evaporation of rubrene in ambient nitrogen using a hot plate delivered the features (highest FL quantum yield and longest FL lifetime) that most resemble those of an amorphous rubrene film. Explicitly, rubrene evaporation on a Peltier-cooled substrate pre-coated with a sensitizer layer and later annealing resulted in enhanced

6320 | *J. Mater. Chem. C*, 2022, **10**, 6314–6322

This journal is © The Royal Society of Chemistry 2022

FL quantum yield ($\phi_{\text{FL}} \approx 15\%$) and triplet energy transfer ($\phi_{\text{TET}} = 60\%$), which enabled reaching a record-high NIR-to-vis UC quantum yield of $(1.2 \pm 0.15)\%$ (out of a maximum of 50%). The attained UC yield is at least 2-fold higher than for any other binary UC film reported so far that is capable of upconverting NIR radiation (>700 nm). Furthermore, the f factor describing the probability for a singlet to be created from two triplets *via* TTA in rubrene films ($f = 19.5\%$) was found to be close to that estimated for rubrene in a solution.[22] Assuming all the intermediate energy transfer processes are 100% efficient, the latter result implies a maximum UC quantum yield of $1/2 \times f \approx 10\%$ thereby also explaining why there are no reports on rubrene UC systems exceeding this value.

Conflicts of interest

There are no conflicts to declare.

Acknowledgements

Notes and references

1 B. D. Ravetz, A. B. Pun, E. M. Churchill, D. N. Congreve, T. Rovis and L. M. Campos, *Nature*, 2019, **565**, 343–346.

2 R. S. Khnayzer, J. Blumhoff, J. A. Harrington, A. Haefele, F. Deng and F. N. Castellano, *Chem. Commun.*, 2011, **48**, 209–211.

3 A. L. Hagstrom, S. Weon, W. Choi and J.-H. Kim, *ACS Appl. Mater. Interfaces*, 2019, **11**, 13304–13318.

4 Y. I. Park, K. T. Lee, Y. D. Suh and T. Hyeon, *Chem. Soc. Rev.*, 2015, **44**, 1302–1317.

5 J. Pedrini and A. Monguzzi, *J. Photonics Energy*, 2017, **8**, 022005.

6 L. Frazer, J. K. Gallaher and T. W. Schmidt, *ACS Energy Lett.*, 2017, **2**, 1346–1354.

7 T. F. Schulze and T. W. Schmidt, *Energy Environ. Sci.*, 2015, **8**, 103–125.

8 V. Gray, K. Moth-Poulsen, B. Albinsson and M. Abrahamsson, *Coord. Chem. Rev.*, 2018, **362**, 54–71.

9 A. Khare, *J. Alloys Compd.*, 2019, 153214.

10 Y. Y. Cheng, B. Fückel, R. W. MacQueen, T. Khoury, R. G. C. R. Clady, T. F. Schulze, N. J. Ekins-Daukes, M. J. Crossley, B. Stannowski, K. Lips and T. W. Schmidt, *Energy Environ. Sci.*, 2012, **5**, 6953–6959.

11 R. A. S. Ferreira, S. F. H. Correia, A. Monguzzi, X. Liu and F. Meinardi, *Mater. Today*, 2020, **33**, 105–121.

12 J. C. Goldschmidt and S. Fischer, *Adv. Opt. Mater.*, 2015, **3**, 510–535.

13 J. Zhou, Q. Liu, W. Feng, Y. Sun and F. Li, *Chem. Rev.*, 2015, **115**, 395–465.

14 P. Bharmoria, H. Bildirir and K. Moth-Poulsen, *Chem. Soc. Rev.*, 2020, **49**, 6529–6554.

15 L. Huang, Y. Zhao, H. Zhang, K. Huang, J. Yang and G. Han, *Angew. Chem., Int. Ed.*, 2017, **56**, 14400–14404.

16 Q. Liu, W. Wang, C. Zhan, T. Yang and D. S. Kohane, *Nano Lett.*, 2016, **16**, 4516–4520.

17 D. Yildiz, C. Baumann, A. Mikosch, A. J. C. Kuehne, A. Herrmann and R. Göstl, *Angew. Chem., Int. Ed.*, 2019, **58**, 12919–12923.

18 S.-W. Liu, C.-C. Lee, C.-H. Yuan, W.-C. Su, S.-Y. Lin, W.-C. Chang, B.-Y. Huang, C.-F. Lin, Y.-Z. Lee, T.-H. Su and K.-T. Chen, *Adv. Mater.*, 2015, **27**, 1217–1222.

19 Y. Zhou, S.-T. Han, X. Chen, F. Wang, Y.-B. Tang and V. a. L. Roy, *Nat. Commun.*, 2014, **5**, 4720.

20 T. Jia, Q. Wang, M. Xu, W. Yuan, W. Feng and F. Li, *Chem. Commun.*, 2021, **57**, 1518–1521.

21 Y. Zhou, F. N. Castellano, T. W. Schmidt and K. Hanson, *ACS Energy Lett.*, 2020, 2322–2326.

22 E. Radiunas, S. Raišys, S. Juršėnas, A. Jozeliūnaitė, T. Javorskis, U. Šinkevičiūtė, E. Orentas and K. Kazlauskas, *J. Mater. Chem. C*, 2020, **8**, 5525–5534.

23 D. G. Bossanyi, Y. Sasaki, S. Wang, D. Chekulaev, N. Kimizuka, N. Yanai and J. Clark, *JACS Au*, 2021, **1**, 2188–2201.

24 Y. Y. Cheng, T. Khoury, R. G. C. R. Clady, M. J. Y. Tayebjee, N. J. Ekins-Daukes, M. J. Crossley and T. W. Schmidt, *Phys. Chem. Chem. Phys.*, 2009, **12**, 66–71.

25 S. Hoseinkhani, R. Tubino, F. Meinardi and A. Monguzzi, *Phys. Chem. Chem. Phys.*, 2015, **17**, 4020–4024.

26 K. M. Felter, M. C. Fravventura, E. Koster, R. D. Abellon, T. J. Savenije and F. C. Grozema, *ACS Energy Lett.*, 2019, 124–129.

27 M. Wu, D. N. Congreve, M. W. B. Wilson, J. Jean, N. Geva, M. Welborn, T. Van Voorhis, V. Bulović, M. G. Bawendi and M. A. Baldo, *Nat. Photonics*, 2016, **10**, 31–34.

28 M. Wu, J. Jean, V. Bulović and M. A. Baldo, *Appl. Phys. Lett.*, 2017, **110**, 211101.

29 S. Amemori, Y. Sasaki, N. Yanai and N. Kimizuka, *J. Am. Chem. Soc.*, 2020, **142**, 8057–8058.

30 L. Nienhaus, J.-P. Correa-Baena, S. Wieghold, M. Einzinger, T.-A. Lin, K. E. Shulenberger, N. D. Klein, M. Wu, V. Bulović, T. Buonassisi, M. A. Baldo and M. G. Bawendi, *ACS Energy Lett.*, 2019, **4**, 888–895.

31 L. Nienhaus, M. Wu, N. Geva, J. J. Shepherd, M. W. B. Wilson, V. Bulović, T. Van Voorhis, M. A. Baldo and M. G. Bawendi, *ACS Nano*, 2017, **11**, 7848–7857.

32 A. Abulikemu, Y. Sakagami, C. Heck, K. Kamada, H. Sotome, H. Miyasaka, D. Kuzuhara and H. Yamada, *ACS Appl. Mater. Interfaces*, 2019, **11**, 20812–20819.

33 C. J. Imperiale, P. B. Green, E. G. Miller, N. H. Damrauer and M. W. B. Wilson, *J. Phys. Chem. Lett.*, 2019, **10**, 7463–7469.

34 S. N. Sanders, M. K. Gangishetty, M. Y. Sfeir and D. N. Congreve, *J. Am. Chem. Soc.*, 2019, 9180–9184.

35 K. J. Fallon, E. M. Churchill, S. N. Sanders, J. Shee, J. L. Weber, R. Meir, S. Jockusch, D. R. Reichman, M. Y. Sfeir, D. N. Congreve and L. M. Campos, *J. Am. Chem. Soc.*, 2020, **142**, 19917–19925.

This journal is © The Royal Society of Chemistry 2022

J. Mater. Chem. C, 2022, **10**, 6314–6322 | 6321

36 V. Yakutkin, S. Aleshchenkov, S. Chernov, T. Miteva, G. Nelles, A. Cheprakov and S. Baluschev, *Chem. – Eur. J.*, 2008, **14**, 9846–9850.

37 T. N. Singh-Rachford and F. N. Castellano, *J. Phys. Chem. A*, 2008, **112**, 3550–3556.

38 Y. Y. Cheng, B. Fückel, T. Khoury, R. G. C. R. Clady, M. J. Y. Tayebjee, N. J. Ekins-Daukes, M. J. Crossley and T. W. Schmidt, *J. Phys. Chem. Lett.*, 2010, **1**, 1795–1799.

39 J. Han, F. Zhang, J. You, Y. Hiroaki, S. Yamada, T. Morifuji, S. Wang and X. Li, *Photochem. Photobiol. Sci.*, 2017, **16**, 1384–1390.

40 A. S. Bieber, Z. A. VanOrman, S. Wieghold and L. Nienhaus, *J. Chem. Phys.*, 2020, **153**, 084703.

41 Y. Che, W. Yang, G. Tang, F. Dumoulin, J. Zhao, L. Liu and Ü. İşci, *J. Mater. Chem. C*, 2018, **6**, 5785–5793.

42 A. B. Pun, L. M. Campos and D. N. Congreve, *J. Am. Chem. Soc.*, 2019, **141**, 3777–3781.

43 E. Radiunas, M. Dapkevičius, S. Raišys, S. Juršėnas, A. Jozeliūnaitė, T. Javorskis, U. Šinkevičiūtė, E. Orentas and K. Kazlauskas, *Phys. Chem. Chem. Phys.*, 2020, **22**, 7392–7403.

44 E. Radiunas, M. Dapkevičius, L. Naimovičius, P. Baronas, S. Raišys, S. Juršėnas, A. Jozeliūnaitė, T. Javorskis, U. Šinkevičiūtė, E. Orentas and K. Kazlauskas, *J. Mater. Chem. C*, 2021, **9**, 4359–4366.

45 D. G. Bossanyi, Y. Sasaki, S. Wang, D. Chekulaev, N. Kimizuka, N. Yanai and J. Clark, *J. Mater. Chem. C*, 2022, **10**, 4684–4696.

46 M. Kinoshita, Y. Sasaki, S. Amemori, N. Harada, Z. Hu, Z. Liu, L. K. Ono, Y. Qi, N. Yanai and N. Kimizuka, *ChemPhotoChem*, 2020, **4**, 5271–5278.

47 S. R. Pristash, K. L. Corp, E. J. Rabe and C. W. Schlenker, *ACS Appl. Energy Mater.*, 2020, **3**, 19–28.

48 S. Wieghold, A. S. Bieber, Z. A. VanOrman and L. Nienhaus, *J. Phys. Chem. Lett.*, 2019, **10**, 3806–3811.

49 K. Seki, T. Yoshida, T. Yago, M. Wakasa and R. Katoh, *J. Phys. Chem. C*, 2021, **125**, 3295–3304.

50 D. M. Finton, E. A. Wolf, V. S. Zoutenbier, K. A. Ward and I. Biaggio, *AIP Adv.*, 2019, **9**, 095027.

51 S.-W. Park, J.-M. Choi, K. H. Lee, H. W. Yeom, S. Im and Y. K. Lee, *J. Phys. Chem. B*, 2010, **114**, 5661–5665.

52 N. Geva, L. Nienhaus, M. Wu, V. Bulović, M. A. Baldo, T. Van Voorhis and M. G. Bawendi, *J. Phys. Chem. Lett.*, 2019, **10**, 3147–3152.

53 L. Wang, J. J. Yoo, T.-A. Lin, C. F. Perkinson, Y. Lu, M. A. Baldo and M. G. Bawendi, *Adv. Mater.*, 2021, e2100854.